Nonsymmetric nonlinear dynamics of piezoelectrically actuated beams

Mergen H. Ghayesh [a,*], Hamed Farokhi [b]

[a] *School of Mechanical Engineering, University of Adelaide, South Australia 5005, Australia*
[b] *Department of Mechanical and Construction Engineering, Northumbria University, Newcastle upon Tyne NE1 8ST, UK*
**Corresponding author: mergen.ghayesh@adelaide.edu.au*
Email: (H Farokhi): hamed.farokhi@northumbria.ac.uk

Abstract

The nonlinear behaviour of a piezoelectrically actuated clamped-clamped beam has been examined numerically while highlighting the nonsymmetric response of the system. The nonlinearly coupled electromechanical model of the piezoelectric-beam system is developed employing the Bernoulli-Euler theory along with the piezoelectric stress-voltage equations. A general nonsymmetric configuration is considered with a piezoelectric patch partially covering the beam. The geometric nonlinearities of stretching type are taken into account for both piezoelectric patch and the beam. Through use of the generalised Hamilton's principle, the nonlinearly coupled electromechanical equations of transverse and longitudinal motions of the piezoelectrically actuated beam are derived. A high-dimensional Galerkin scheme is utilised to recast the equations of partial differential type into ordinary differential type. For comparison and benchmark purposes, a three-dimensional finite element model is developed in Abaqus/CAE to verify the model developed in this study. It is shown that the response of the system is strongly nonsymmetric and that it is essential to retain many degrees of freedom to ensure converged results.

Keywords: Piezoelectrically actuated; Nonsymmetric motion; Nonlinear oscillation; Finite element analysis

1. Introduction

Piezoelectrics are commonly used as convenient tools for sensing and actuations in many engineering systems and applications. In particular, they are used for position control, active vibration isolators, static and dynamic actuations, and energy harvesting. The coupled electromechanical nature of piezoelectrics, along with geometric nonlinearities arising in many engineering applications, makes the modelling and analysis of such systems a complicated task.

There are many studies in the literature on applications of piezoelectrics in actuation, sensing, control, and energy harvesting [1-9]. For instance, Want and Quek [10] developed a basic mechanics model for the linear flexural analysis of an Euler-Bernoulli beam coupled with a piezoelectric actuator. Lee et al. [11] proposed, fabricated and characterized piezoelectrically actuated radio-frequency microelectromechanical system (MEMS) switches, operating at a low voltage for advanced handset applications. Further studies were conducted by Narita et al. [12], who conducted analytical and experimental investigations on the nonlinear bending behaviour of laminated piezoelectric actuators as a function of the amplitude and frequency of the electric field. Kumar and Narayanan [2] conducted an analysis, based on a finite element (FE) technique, on control of vibration of a beam through optimised positioning of sensor and actuator of piezoelectric type. The investigations were continued by Ghazavi et al. [13] who performed a stability analysis on the transverse response of a cantilevered microscale beam actuated by piezoelectric patches attached to the top and bottom surfaces of the beam. Bowen et al. [14] developed an FE model to predict the snap-through of asymmetric piezoelectrically actuated bistable laminates; they modelled the deflection of an actuated aluminium beam and compared it to

experimental observation. Further investigations were conducted by Mahmoodi et al. [15], who examined the subharmonic resonant flexural vibrations of piezoelectrically actuated microcantilevers; they used a one-mode Galerkin discretisation as well as the multiple scales method to examine the system response analytically; Kumar et al. [16], who utilised piezoelectrically actuated microcantilevers for mass sensing applications; and Xiao et al. [17], who analysed the size-dependent static pull-in behaviour of an electrostatically actuated MEMS consisting of piezoelectric layers. All of these valuable studies are either based on experimental observations, static numerical analysis, or low-dimensional/single-mode dynamic numerical analysis. Additionally, several researchers have developed nonlinear electromechanical models for the purpose of studying the nonsymmetric behaviour of a piezoelectric beam. For instance, He and Daqaq [18] examined the effect of potential function's asymmetries on the power output of vibration energy harvesters under white noise excitations; they showed that the asymmetries in the potential function improve the performance of the vibration energy harvester under white noise. Leadenham and Erturk [19] investigated the nonlinear dynamic characteristics of a piezoelectric cantilever subject to relatively high electrical and mechanical excitation magnitudes in sensing and actuation as well as in energy harvesting; they conducted both theoretical and experimental analysis on a piezoelectric cantilever and found great agreement between the proposed model and experimental results. Wang et al. [20] studied the performance enhancement of a cantilever energy harvester with nonsymmetric potentials; they constructed the bifurcation diagrams to examine the influence of nonsymmetric potentials on the output response.

In this research, for the first time, a high-dimensional nonlinear electromechanical model is developed for analysing the nonsymmetric nonlinear behaviour of a piezoelectrically actuated clamped-clamped beam in both static and dynamic regimes. It is shown that due to nonsymmetric configuration of the system and the presence of geometric nonlinearities, a large number of modes are required to ensure converged results. The developed model is validated for the nonlinear static response via three-dimensional finite element analysis. The nonlinear primary and secondary resonance responses of the piezoelectrically actuated beam are examined in detail showing complex resonance responses and strong modal interactions. Time histories and phase-plane portraits in regions of interest are plotted as well to give more insight to the dynamical behaviour of the system.

2. Coupled electromechanical model development

Figure 1 illustrates the schematic representation of a piezoelectrically actuated clamped-clamped beam. As seen, the beam is of length L, width b, and thickness t_b, while the piezoelectric patch is of length l_2-l_1 and thickness t_p. The cross-sectional area and second moment of area of the beam are represented by A_b and I_b, respectively; the cross-sectional area of the piezoelectric patch is denoted by A_p. The coupled system motion is described in Cartesian coordinates, with x and z denoting the axial and transverse directions. The displacements of the beam centreline are shown by $u(x,t)$, for movement in the x direction, and $w(x,t)$, for movement in the z direction; t stands for time.

In what follows, the beam theory of Euler-Bernoulli and the one-dimensional constitutive piezoelectric equations are employed to develop a geometrically nonlinear model of the piezoelectrically actuated clamped-clamped beam.

The geometrically nonlinear strain-displacement for both beam and piezoelectric can be expressed as

$$\varepsilon_{xx} = \varepsilon_1 = \begin{cases} \dfrac{\partial u}{\partial x} - z\dfrac{\partial^2 w}{\partial x^2} + \dfrac{1}{2}\left(\dfrac{\partial w}{\partial x}\right)^2 & x > l_2 \text{ or } x < l_1, \\ \dfrac{\partial u}{\partial x} - (z - z_n)\dfrac{\partial^2 w}{\partial x^2} + \dfrac{1}{2}\left(\dfrac{\partial w}{\partial x}\right)^2 & l_1 \le x \le l_2, \end{cases} \tag{1}$$

where z_n is the neutral axis for the piezo-attached part of the beam, measured from the beam centreline.

The axial stress in the beam can be formulated as:

$$\sigma_b = E_b \varepsilon_{xx}, \tag{2}$$

in which E_b denotes the Young's modulus of the beam.

The piezoelectric equations for the configuration shown in Fig. 1 are given by

$$\begin{aligned} \sigma_p &= c_{11}^D \varepsilon_1 - h_{31} D_3, \\ E_3 &= -h_{31}\varepsilon_1 + \beta_{33} D_3, \end{aligned} \tag{3}$$

with the subscripts 1 and 3 denoting the x and z directions. The piezoelectric poling direction is assumed to be in the positive z direction. Additionally, E_3 and D_3 denote the electric field and the dielectric displacement in the z direction, respectively, c_{11}^D represents

the elastic stiffness coefficient under constant dielectric displacement, β_{33} stands for the impermittivity constant. h_{31} is a piezoelectric constant that will be defined later.

The variation of the elastic potential energy of the piezoelectric-beam system is given by

$$\begin{aligned}\delta\Pi &= \delta\Pi_{\text{beam}} + \delta\Pi_{\text{piezo}} \\ &= \int_V \left(\sigma_b \delta\varepsilon_{xx}\right) \mathrm{d}V + \int_V \left(\sigma_p \delta\varepsilon_{xx} + E_3 \delta D_3\right) \mathrm{d}V \\ &= \int_V \left(\sigma_b \delta\varepsilon_{xx}\right) \mathrm{d}V + \int_V \left[\left(c_{11}^D \varepsilon_1 - h_{31} D_3\right)\delta\varepsilon_{xx} + \left(-h_{31}\varepsilon_1 + \beta_{33}^S D_3\right)\delta D_3\right] \mathrm{d}V.\end{aligned} \tag{4}$$

Next, the electrical virtual work as a result of the input voltage to the piezoelectric patch is modelled. The sign of the external electrical work depends on the input voltage being applied to the top or bottom surface of the piezoelectric patch. In this study, it is assumed that an input voltage V is exerted to the upper surface of the piezoelectric patch, resulting in a virtual electrical work of

$$\delta W_{ext} = -b\int_0^L \left[V(x,t)\,\delta D_3(x,t)\right] \mathrm{d}x. \tag{5}$$

The variation of the piezoelectric-beam motion energy is given by

$$\delta KE = \int_0^L m(x)\left[\frac{\partial}{\partial t}(\delta w)\frac{\partial w}{\partial t} + \frac{\partial}{\partial t}(\delta u)\frac{\partial u}{\partial t}\right] \mathrm{d}x, \tag{6}$$

in which

$$\begin{aligned} m(x) &= b\left(\rho_b t_b + G(x)\rho_p t_p\right) = \rho_b A_b + G(x)\rho_p A_p, \\ G(x) &= H(x-l_1) - H(x-l_2), \end{aligned} \tag{7}$$

where ρ_b and ρ_p are the beam and piezoelectric densities, respectively, and $H(x)$ is the Heaviside function defined as

$$H(x-x_0)=\begin{cases}1 & x\geq x_0,\\ 0 & x<x_0.\end{cases} \tag{8}$$

The virtual work of a viscous damping mechanism can be expressed as

$$\delta W_v=-\int_0^L c_d(x)\left[\delta w\frac{\partial w}{\partial t}+\delta u\frac{\partial u}{\partial t}\right]\mathrm{d}x, \tag{9}$$

where $c_d(x)=c_d^b+c_d^pG(x)$, with c_d^b and c_d^p being respectively the beam and piezoelectric patch viscous damping coefficients.

Substitution of Eqs. (4-6) and (9) into generalised Hamilton's principle and setting the coefficients of δu, δw, and δD_3 equal to zero gives

$$m(x)\frac{\partial^2 u}{\partial t^2}+c_d(x)\frac{\partial u}{\partial t}-\frac{\partial}{\partial x}\left[e(x)\left(\frac{\partial u}{\partial x}+\frac{1}{2}\left(\frac{\partial w}{\partial x}\right)^2\right)\right]-\frac{\partial}{\partial x}\left[f(x)\frac{\partial^2 w}{\partial x^2}\right]+\frac{\partial}{\partial x}\left[h_2(x)D_3\right]=0, \tag{10}$$

$$\begin{aligned}&m(x)\frac{\partial^2 w}{\partial t^2}+\frac{\partial^2}{\partial x^2}\left[C(x)\frac{\partial^2 w}{\partial x^2}\right]+c_d(x)\frac{\partial w}{\partial t}-\frac{\partial}{\partial x}\left[e(x)\left(\frac{\partial w}{\partial x}\right)\left(\frac{\partial u}{\partial x}+\frac{1}{2}\left(\frac{\partial w}{\partial x}\right)^2\right)\right]\\ &-\frac{\partial}{\partial x}\left[f(x)\frac{\partial w}{\partial x}\frac{\partial^2 w}{\partial x^2}\right]+\frac{\partial^2}{\partial x^2}\left[f(x)\left(\frac{\partial u}{\partial x}+\frac{1}{2}\left(\frac{\partial w}{\partial x}\right)^2\right)\right]\\ &+\frac{\partial^2}{\partial x^2}\left[h_1(x)D_3\right]+\frac{\partial}{\partial x}\left[\left(\frac{\partial w}{\partial x}\right)h_2(x)D_3\right]=0,\end{aligned} \tag{11}$$

$$h_1(x)\frac{\partial^2 w}{\partial x^2}-h_2(x)\left(\frac{\partial u}{\partial x}+\frac{1}{2}\left(\frac{\partial w}{\partial x}\right)^2\right)+\beta(x)D_3+bV(x,t)=0. \tag{12}$$

$D_3(x,t)$ can be calculated explicitly using Eq. (12) and substituted into Eqs. (10) and (11); this procedure results in the final nonlinearly coupled equations of the piezoelectrically actuated system

$$
\begin{aligned}
&m(x)\frac{\partial^2 u}{\partial t^2}+c_d(x)\frac{\partial u}{\partial t}-\frac{\partial}{\partial x}\left[\left(e(x)-\frac{h_2(x)^2}{\beta(x)}\right)\left(\frac{\partial u}{\partial x}+\frac{1}{2}\left(\frac{\partial w}{\partial x}\right)^2\right)\right]\\
&-\frac{\partial}{\partial x}\left[\left(f(x)+\frac{h_1(x)h_2(x)}{\beta(x)}\right)\frac{\partial^2 w}{\partial x^2}\right]-\frac{\partial}{\partial x}\left[V(x,t)\frac{bh_2(x)}{\beta(x)}\right]=0,
\end{aligned}
\tag{13}
$$

$$
\begin{aligned}
&m(x)\frac{\partial^2 w}{\partial t^2}+c_d(x)\frac{\partial w}{\partial t}+\frac{\partial^2}{\partial x^2}\left[\frac{\partial^2 w}{\partial x^2}\left(C(x)-\frac{h_1(x)^2}{\beta(x)}\right)\right]\\
&-\frac{\partial}{\partial x}\left[\left(e(x)-\frac{h_2(x)^2}{\beta(x)}\right)\left(\frac{\partial w}{\partial x}\right)\left(\frac{\partial u}{\partial x}+\frac{1}{2}\left(\frac{\partial w}{\partial x}\right)^2\right)\right]\\
&+\frac{\partial^2}{\partial x^2}\left[\left(\frac{1}{2}\left(\frac{\partial w}{\partial x}\right)^2+\frac{\partial u}{\partial x}\right)\left(f(x)+\frac{h_2(x)}{\beta(x)}h_1(x)\right)\right]-\frac{\partial}{\partial x}\left[\left(\frac{\partial^2 w}{\partial x^2}\frac{\partial w}{\partial x}\right)\left(f(x)+\frac{h_2(x)}{\beta(x)}h_1(x)\right)\right]\\
&-\frac{\partial^2}{\partial x^2}\left[\frac{b}{\beta(x)}h_1(x)V(x,t)\right]-\frac{\partial}{\partial x}\left[V(x,t)\frac{bh_2(x)}{\beta(x)}\left(\frac{\partial w}{\partial x}\right)\right]=0,
\end{aligned}
\tag{14}
$$

in which

$$
\begin{aligned}
&C(x)=E_bI_b+G(x)\left\{E_bA_bz_z^2+\frac{1}{3}bc_{11}^D\left[t_p^3+3t_p\left(\frac{t_b}{2}-z_n\right)^2+3t_p^2\left(\frac{t_b}{2}-z_n\right)\right]\right\},\\
&e(x)=E_bA_b+c_{11}^DA_pG(x),\\
&f(x)=G(x)\left[E_bA_bz_n+c_{11}^DA_p\left(z_n-\frac{1}{2}\left(t_b+t_p\right)\right)\right],\\
&h_1(x)=\frac{1}{2}A_ph_{31}\left(t_b+t_p-2z_n\right)G(x),\\
&h_2(x)=A_ph_{31}G(x),\\
&\beta(x)=A_p\beta_{33}G(x),\\
&V(x,t)=V(t)G(x).
\end{aligned}
\tag{15}
$$

Equations (13) and (14) represent the continuous model of the clamped-clamped piezoelectrically actuated beam while accounting for both longitudinal and transverse

displacements as well as the geometric nonlinearities arising from midplane stretching. In what follows, the motion equations are reduced to ordinary differential equations (ODEs) via application of the Galerkin method. To this end, the displacements are defined as a summation of functions of *x* multiplied by generalised coordinates, which are functions of time. Given that the system under consideration is clamped at both ends, the eigenfunctions of doubly clamped beam for the axial motion, denoted by X, and transverse motion, denoted by Ψ, are selected as the shape functions in the Galerkin technique. Hence, denoting the generalised coordinates associated with the longitudinal and transverse displacements by *r* and *q*, respectively, the system displacements can be approximated as

$$u=\sum_{m=1}^{M}\mathrm{X}_m(x)r_m(t),$$
$$w=\sum_{n=1}^{N}\Psi_n(x)q_n(t). \tag{16}$$

The expressions for the trial functions X_m and Ψ_n are given by

$$\mathrm{X}_m(x)=\sin\left(\frac{m\pi x}{L}\right), \tag{17}$$

$$\Psi_n(x)=\left[\cosh\left(\frac{\theta_n x}{L}\right)-\chi_n\sinh\left(\frac{\theta_n x}{L}\right)\right]-\left[\cos\left(\frac{\theta_n x}{L}\right)-\chi_n\sin\left(\frac{\theta_n x}{L}\right)\right],$$
$$\chi_n=\frac{\cos(\theta_n)-\cosh(\theta_n)}{\sin(\theta_n)-\sinh(\theta_n)}, \tag{18}$$

where θ_n is the *n*th root the equation $1-\cos(\theta)\cosh(\theta)=0$. Substituting the displacement series expansions into equations of motion and following the rest of the Galerkin scheme procedure yields discretised motion equations, i.e. a set of ODES of dimension *M*+*N*. In the

numerical calculations conducted in this study, *M* and *N* are set to 16, i.e. a 32-degree-of-freedom (32-DOF) model, which ensures converged results (please see Appendix A for the convergence analysis). This high-dimensional set of ODEs is solved numerically making use of a well-optimised continuation technique as well as an optimised time-integration method.

3. Numerical results and discussions

In this section, the numerical calculations are conducted considering both static and dynamic actuation cases. For the cases examined in this section, t_b= t_p =0.5 mm, b=6t_b, L=200t_b, l_1=0.1L, and l_2=0.5L. For the case of static analysis, the nonlinear deflection of the system is obtained using two models, i.e. the model developed in this study and a three-dimensional (3D) finite element model (FEM) developed in Abaqus/CAE. The beam is assumed to be made of Aluminium of E_b=70 GPa, ρ_b=2300 kg/m^3, and Poisson's ratio ν_b=0.33. The piezoelectric material is assumed to be Lead Zirconate Titanate (PZT-5H) of ρ_p=7500 kg/m^3 and other material properties as listed in Table 1. It should be noted that the properties given in Table 1 are for the piezoelectric strain-charge constitutive form while the stress-voltage constitutive form is used in Section 2 for modelling. Hence, the constants in Eq. (3) can be obtained in terms of the piezoelectric material properties given in Table 1 as

$$c_{11}^{D}=\left(s_{11}-\frac{d_{31}^{2}}{\xi_{33}}\right)^{-1},\quad h_{31}=-\left(d_{31}-\frac{s_{11}\xi_{33}}{d_{31}}\right)^{-1},\quad \beta_{33}=\left(\xi_{33}-\frac{d_{31}^{2}}{s_{11}}\right)^{-1}, \tag{19}$$

resulting in $c_{11}^{D} = 71.3973$ GPa, h_{31}=-649.8374×10^6 V/m, and β_{33}=39.1325×10^6 m/F.

3.1 Nonlinear static response

The nonlinear static deflection of the piezoelectrically actuated beam when a DC input voltage of amplitude V_s is applied to the piezoelectric patch. As mentioned before, the nonlinear static results are obtained employing the model developed in Section 2 as well as using finite element (FE) analysis. The geometrically nonlinear FE analysis is conducted in Abaqus/CAE using C3D20R element (i.e. a 20-node three-dimensional element) for the beam and C3D20RE element (i.e. a 20-node piezoelectric three-dimensional element) for the piezoelectric patch.

An important point to mention and discuss here is the correct value of z_n, i.e. the location of the neutral axis. Care should be taken when setting the value of z_n depending on the type of analysis being performed. In case of a linear analysis, the location of the neutral axis changes in the portion of the beam covered by the piezoelectric patch. When examining the nonlinear response of a clamped-clamped beam, the main source of nonlinearity is the centreline stretching; in fact, due to stretching of the centreline, there is not point on the beam cross-section on which the stress is zero. A comparison of the nonlinear static response of the piezoelectrically actuated beam with nonlinear 3D finite element analysis reveals that the best results are obtained when z_n =0, i.e. the integration over the thickness in the partially covered portion of the beam is conducted with reference to the beam centreline.

A comparison between the deformed configuration of the piezoelectrically actuated system obtained via the present model and the 3D FE model is shown in Fig. 2 for both transverse and longitudinal displacements for two different input voltage amplitudes. It should be noted that the transverse and longitudinal displacements are plotted for top beam surface, i.e. at $z=t_b/2$. For the beam theory employed in this study, the displacement in the transverse direction is the same throughout the thickness ($U_3=w$); however, the longitudinal displacement at $z=t_b/2$ is obtained as $U_1 = u-(t_b/2)\partial w/\partial x$. As seen, the model developed in this study predicts almost the same transverse displacement as the nonlinear 3D finite element model; furthermore, the predicted longitudinal displacement is also very similar to that obtained using 3D FEM, showing the high accuracy of the model developed in this study.

Figure 3 illustrates the nonlinear static transverse displacement of the piezoelectrically actuated beam at $x/L=0.3$ obtained via the developed model and the 3D FEM. As seen, the predictions of the developed beam model match those of the 3D finite element analysis. Furthermore, the figure shows that the system exhibits a nonlinear behaviour as a result of centreline stretching nonlinearity. The contour plots of the 3D finite element analysis are shown in Fig. 4 for the transverse displacement, $U_3=w$.

3.2 Nonlinear resonance dynamics

This section analyses the nonlinear resonance dynamical characteristics of the piezoelectrically actuated beam when an AC input voltage, i.e. $V(t)=V_d\cos(\omega_p t)$, is applied to the piezoelectric patch. In the numerical calculations, the time (t), excitation frequency (ω_p),

transverse natural frequencies ($\hat{\omega}_i$), and damping coefficient ($c_d = c_d^b = c_d^p$) are made dimensionless as

$$\tau = t\sqrt{\frac{E_b I_b}{\rho_b A_b L^4}},\ \ \Omega_p = \omega_p \sqrt{\frac{\rho_b A_b L^4}{E_b I_b}}, \qquad \omega_i = \hat{\omega}_i \sqrt{\frac{\rho_b A_b L^4}{E_b I_b}}\ \ i = 1,2, \qquad c_d^* = \frac{c_d L^4}{E_b I_b}\sqrt{\frac{E_b I_b}{\rho_b A_b L^4}} \tag{20}$$

in which the quantities on the left-hand side are dimensionless. In this study, c_d^* is replaced by $2\zeta\omega_1$, where ζ is the modal damping ratio, set to 0.006 for all results. In all the frequency- and force-amplitude plots of this section, stable solution is shown by solid line and unstable solution is depicted by dashed line.

Two cases of resonance are studied by changing the excitation frequency Ω_p: (i) near ω_1, i.e. the primary resonance, and (ii) near ω_2, i.e. the secondary resonance. Due to the nonsymmetric configuration of the system and the piezoelectric load, the nonsymmetric modes contribute to the nonlinear dynamical behaviour of the system. Hence, in the case of secondary resonance, the system undergoes oscillations of similar amplitudes as the primary resonance case under the same input voltage amplitude.

The frequency-amplitude diagrams for the case of primary resonance are depicted in Fig. 5 for centreline displacements in (a) transverse direction at x/L=0.56 and (b) longitudinal direction at x/L=0.66; V_d = 13.0 V for this case. The selected locations of the displacements correspond to their maximum amplitudes in a period of oscillation. As seen, the piezoelectrically actuated beam displays nonlinear behaviour of hardening-type due to the induced tension caused by centreline stretching of the beam. The presence of hardening nonlinearity causes a hysteresis-type response in the frequency-amplitude of the system. More specifically, when a frequency-sweep in the right direction on the frequency axis is

conducted, the system response amplitude increases accordingly until reaching a limit point at Ω_p/ω_1=1.1558 where the occurrence of a saddle-node bifurcation causes a sudden drop in the amplitude of the system (drop point). Then if a frequency-sweep in the reverse direction is conducted, a different solution path of smaller amplitude is followed; in this case, a limit point is reached at Ω_p/ω_1=1.0240 where yet another saddle-node bifurcation occurs and the system amplitude increases suddenly.

The frequency-amplitude plots of different generalised coordinates of the system of Fig. 5 are shown in Fig. 6, showing the contribution of the nonsymmetric modes to the response of the system. Additionally, as seen, strong modal interactions are present in the primary resonance region. To better examine the dynamical characteristics of the system, the time histories and phase-plane portraits are plotted in Figs. 7 and 8 for both transverse and longitudinal motions of the system of Fig. 5 at two different excitation frequencies. Figure 7 corresponds to the excitation frequency of Ω_p/ω_1=1.0373, i.e. in the region of strong modal interactions, while Fig. 8 corresponds to the excitation frequency of Ω_p/ω_1=1.1558, i.e. at drop point. In both figures τ_n denotes the normalised time with respect to the period of oscillation. As seen, the system displays more complicated oscillation characteristics when modal interactions are present.

The force-amplitude plots of the piezoelectrically actuated system in the primary resonance region are shown in Fig. 9. To construct the force-amplitude plots, Ω_p/ω_1=1.04 is selected and the input voltage amplitude, i.e. V_d, is changed. As seen, a hysteresis-type behaviour is present here as well where depending on the direction of the force sweep, the system follows a different solution path. Saddle-node bifurcations occur at jump points, i.e.

V_d = 27.2270 and 6.5545. The force-amplitude plots of different generalised coordinates are depicted in Fig. 10, showing again the presence of strong modal interactions.

The frequency-amplitude curves of the piezoelectrically actuated beam in the secondary resonance region are plotted in Fig. 11, when V_d = 13.0 V. Here the maximum transverse and longitudinal displacements in a period of oscillation occur at x/L=0.81 and x/L=0.34, respectively. Similar to the case of primary resonance, the system displays nonlinear hardening behaviour. As seen in the zoomed areas, the presence of modal interactions results in the appearance of extra saddle-node bifurcations in the vicinity of Ω_p/ω_2=1.08. The frequency-amplitude plots of the generalised coordinates of the system of Fig. 11 are shown in Fig. 12; as seen, the amplitude of the second generalised coordinate is more than that of the first generalised coordinate since the system is being excited in the secondary resonance region. The time trace and phase-plane plots of the transverse and longitudinal displacements at Ω_p/ω_2=1.1164 (i.e. the drop point) are shown in Fig. 13.

4. Conclusions

This study examined the nonsymmetric nonlinear behaviour of a piezoelectrically actuated clamped-clamped beam in both static and dynamic regimes. The nonlinear coupled electromechanical model of the piezoelectric-beam system is developed using the nonlinear Euler-Bernoulli theory as well as the piezoelectric equations. The equations of motion of partial differential form are obtained through use of the generalised Hamilton's principle, which are then reduced to ordinary differential form via use of the Galerkin technique. The equations are then solved numerically.

The nonlinear static deflection was examined via a 32-DOF model as well as a 3D finite element model. A comparison of the predictions of the developed model and the 3D FEM showed the great accuracy and reliability of the developed model.

The nonlinear dynamic simulations in the primary resonance regions revealed that the system shows nonlinear characteristic of hardening-type as well as strong interactions between different modes. Additionally, the piezoelectrically actuated beam shows hardening behaviour in the secondary resonance region as well. For the case of secondary resonance, it was shown that the amplitude of the nonsymmetric mode q_2 is more than that of q_1, showing the strong nonsymmetric response of the system. The force-amplitude curves of the system showed the presence of a hysteresis-type behaviour with jumps in the response amplitude at two points; modal interactions were present in the force-response of the piezoelectric-beam system as well.

Appendix A. Convergence analysis

A convergence analysis is conducted in this section to show the importance and necessity of retaining many degrees of freedom in the discretised model. Hence, Fig. 14 is plotted illustrating the nonlinear transverse deflection of the beam under static piezoelectric actuation obtained via 3D finite element model as well as several discretised models of different dimensions. It should be noted that for each discretised model, the number of generalised coordinates is the same for longitudinal and transverse motions.

As seen in Fig. 14, the 4-DOF and 8-DOF models give very inaccurate results. Even the 16-DOF model cannot predict the static response of the system accurately, especially in the range $0.6<x/L<0.9$. The 32-DOF model used in this study, on the other hand, predicts almost the same response as the 3D FE model, showing converged results. This figure signifies the importance of using a high-dimensional discretised model for accurate analysis.

References

[1] Irschik, H., 2002, "A review on static and dynamic shape control of structures by piezoelectric actuation," Engineering Structures, 24(1), pp. 5-11.
[2] Kumar, K. R., and Narayanan, S., 2008, "Active vibration control of beams with optimal placement of piezoelectric sensor/actuator pairs," Smart Materials and Structures, 17(5), p. 055008.
[3] Raja, S., Prathap, G., and Sinha, P., 2002, "Active vibration control of composite sandwich beams with piezoelectric extension-bending and shear actuators," Smart Materials and Structures, 11(1), p. 63.
[4] Vasques, C., and Rodrigues, J. D., 2006, "Active vibration control of smart piezoelectric beams: comparison of classical and optimal feedback control strategies," Computers & structures, 84(22-23), pp. 1402-1414.
[5] Halim, M. A., and Park, J. Y., 2014, "Theoretical modeling and analysis of mechanical impact driven and frequency up-converted piezoelectric energy harvester for low-frequency and wide-bandwidth operation," Sensors and Actuators A: Physical, 208, pp. 56-65.
[6] Hu, G., Tang, L., and Das, R., 2017, "An impact-engaged two-degrees-of-freedom Piezoelectric Energy Harvester for Wideband Operation," Procedia Engineering, 173, pp. 1463-1470.
[7] Huicong, L., Chengkuo, L., Takeshi, K., Cho Jui, T., and Chenggen, Q., 2012, "Investigation of a MEMS piezoelectric energy harvester system with a frequency-widened-bandwidth mechanism introduced by mechanical stoppers," Smart Materials and Structures, 21(3), p. 035005.
[8] Liu, H., Lee, C., Kobayashi, T., Tay, C. J., and Quan, C., 2012, "Piezoelectric MEMS-based wideband energy harvesting systems using a frequency-up-conversion cantilever stopper," Sensors and Actuators A: Physical, 186, pp. 242-248.
[9] Liu, S., Cheng, Q., Zhao, D., and Feng, L., 2016, "Theoretical modeling and analysis of two-degree-of-freedom piezoelectric energy harvester with stopper," Sensors and Actuators A: Physical, 245, pp. 97-105.
[10] Wang, Q., and Quek, S. T., 2000, "Flexural vibration analysis of sandwich beam coupled with piezoelectric actuator," Smart Materials and Structures, 9(1), p. 103.
[11] Lee, H.-C., Park, J.-H., Park, J.-Y., Nam, H.-J., and Bu, J.-U., 2005, "Design, fabrication and RF performances of two different types of piezoelectrically actuated Ohmic MEMS switches," Journal of micromechanics and microengineering, 15(11), p. 2098.
[12] Narita, F., Shindo, Y., and Mikami, M., 2005, "Analytical and experimental study of nonlinear bending response and domain wall motion in piezoelectric laminated actuators under ac electric fields," Acta Materialia, 53(17), pp. 4523-4529.
[13] Ghazavi, M.-R., Rezazadeh, G., and Azizi, S., 2010, "Pure parametric excitation of a micro cantilever beam actuated by piezoelectric layers," Applied Mathematical Modelling, 34(12), pp. 4196-4207.
[14] Bowen, C. R., Giddings, P. F., Salo, A. I., and Kim, H. A., 2011, "Modeling and characterization of piezoelectrically actuated bistable composites," IEEE transactions on ultrasonics, ferroelectrics, and frequency control, 58(9), pp. 1737-1750.
[15] Mahmoodi, S. N., Jalili, N., and Ahmadian, M., 2010, "Subharmonics analysis of nonlinear flexural vibrations of piezoelectrically actuated microcantilevers," Nonlinear Dynamics, 59(3), pp. 397-409.
[16] Kumar, V., Boley, J. W., Yang, Y., Ekowaluyo, H., Miller, J. K., Chiu, G. T.-C., and Rhoads, J. F., 2011, "Bifurcation-based mass sensing using piezoelectrically-actuated microcantilevers," Applied Physics Letters, 98(15), p. 153510.
[17] Xiao, Y., Wang, B., and Zhou, S., 2015, "Pull-in voltage analysis of electrostatically actuated MEMS with piezoelectric layers: a size-dependent model," Mechanics Research Communications, 66, pp. 7-14.

[18] He, Q., and Daqaq, M. F., 2014, "Influence of potential function asymmetries on the performance of nonlinear energy harvesters under white noise," Journal of Sound and Vibration, 333(15), pp. 3479-3489.
[19] Leadenham, S., and Erturk, A., 2015, "Unified nonlinear electroelastic dynamics of a bimorph piezoelectric cantilever for energy harvesting, sensing, and actuation," Nonlinear Dynamics, 79(3), pp. 1727-1743.
[20] Wang, W., Cao, J., Bowen, C. R., Zhang, Y., and Lin, J., 2018, "Nonlinear dynamics and performance enhancement of asymmetric potential bistable energy harvesters," Nonlinear Dynamics, 94(2), pp. 1183-1194.

Table 1. Material properties of the piezoelectric patch (PZT-5H)

Compliance matrix components ($\times 10^{-12}$ m^2/N): s_{11}=16.5, s_{12}=-4.78, s_{13}=-8.45, s_{33}=20.7, s_{44}=43.5
Piezoelectric constans matrix (**d**) components ($\times 10^{-12}$ m/V): d_{31}=-274, d_{33}=593, d_{15}=741
Relative permittivity matrix components (ξ_0 = 8.8542$\times 10^{-12}$ F/m): ξ_{11}/ξ_0 = 3130, ξ_{33}/ξ_0 = 3400

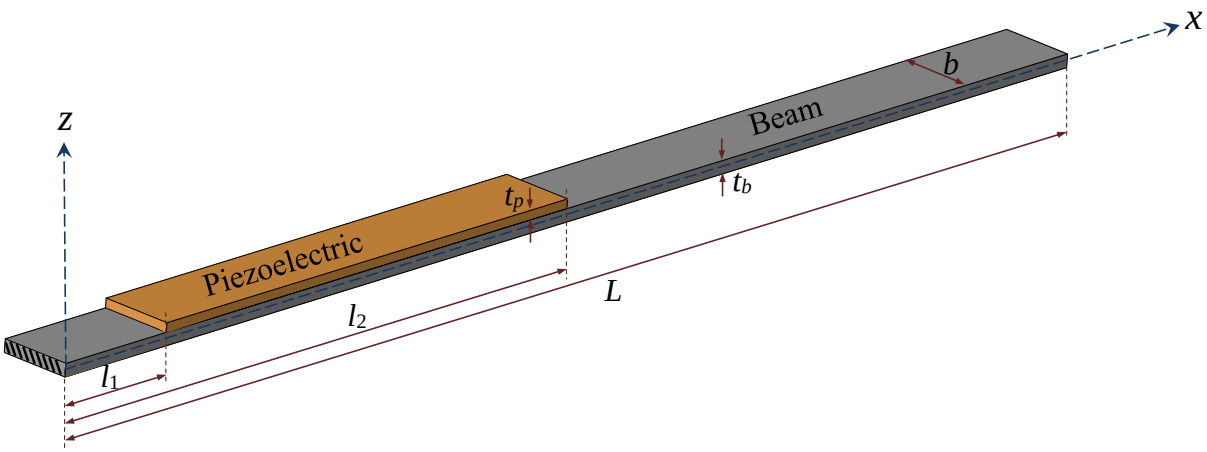

Fig.1. Schematic of a piezoelectrically actuated clamped-clamped beam.

(a)

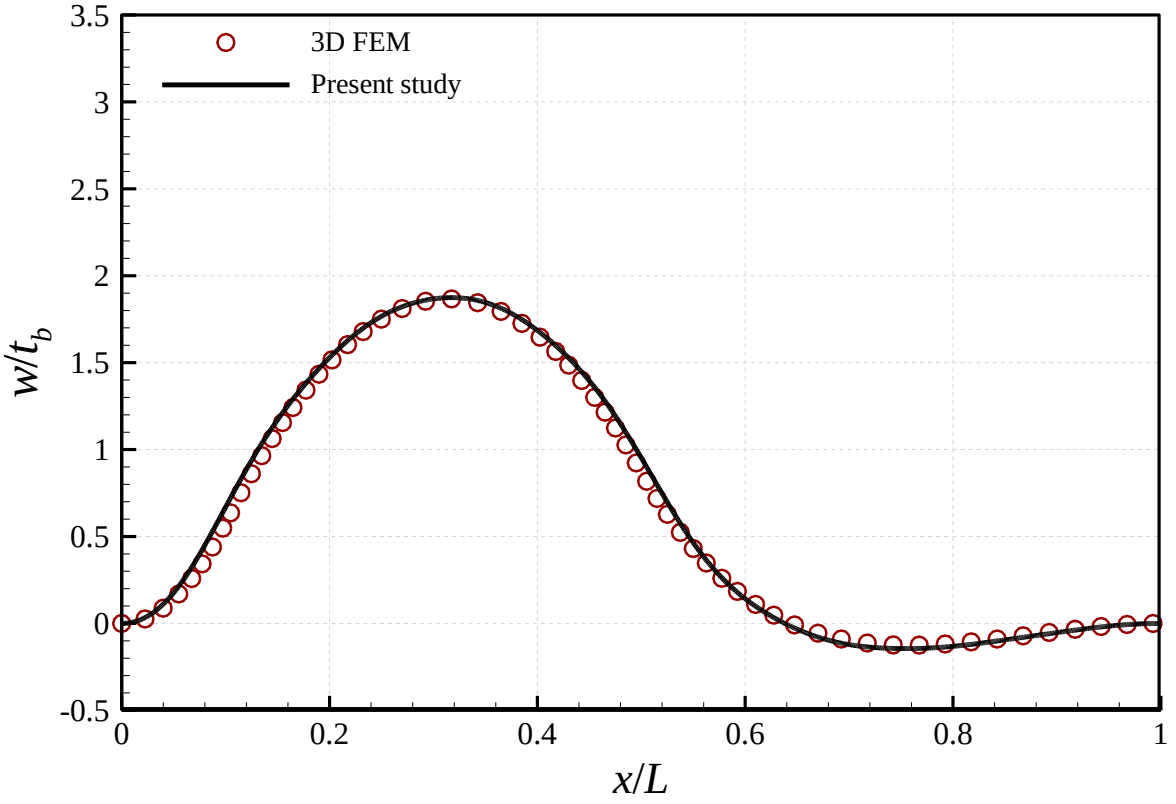
3D FEM
Present study
3.5
3
2.5
2
1.5
1
0.5
0
-0.5
0
0.2
0.4
0.6
0.8
1
w/t_b
x/L

(b)

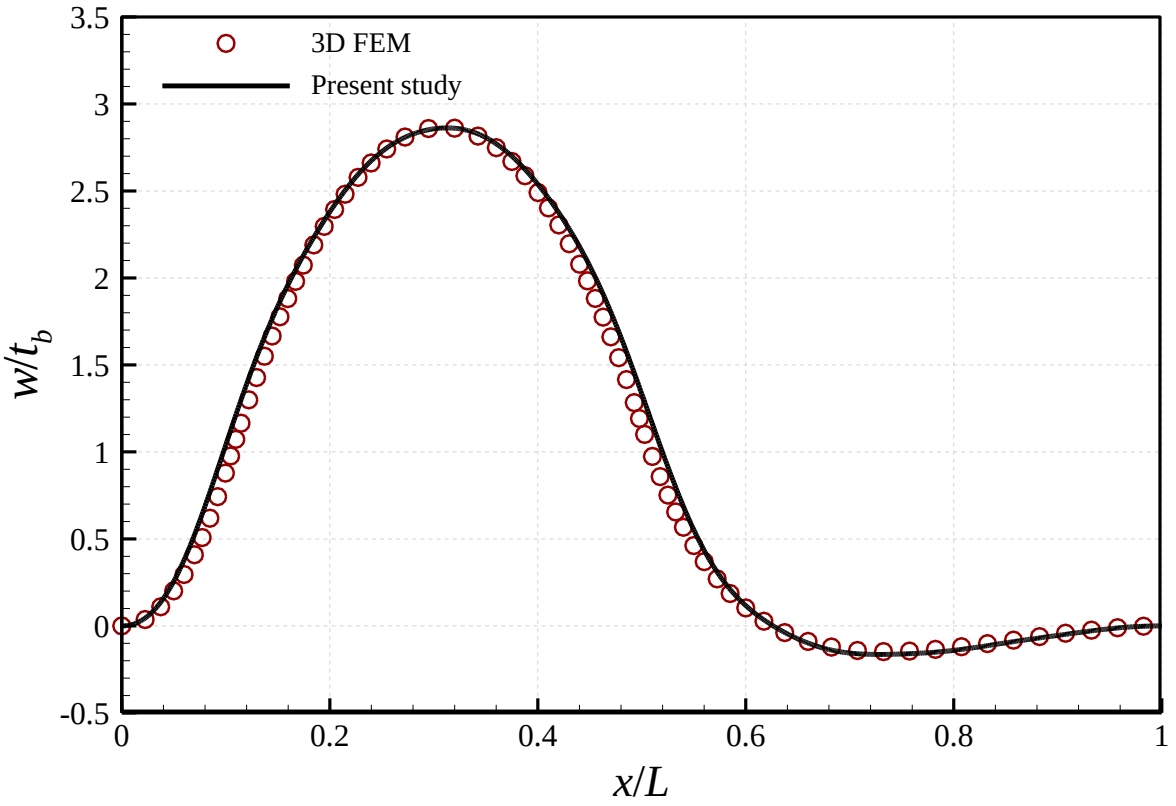
3D FEM
Present study
3.5
3
2.5
2
1.5
1
0.5
0
-0.5
0
0.2
0.4
0.6
0.8
1
w/t_b
x/L

(c)

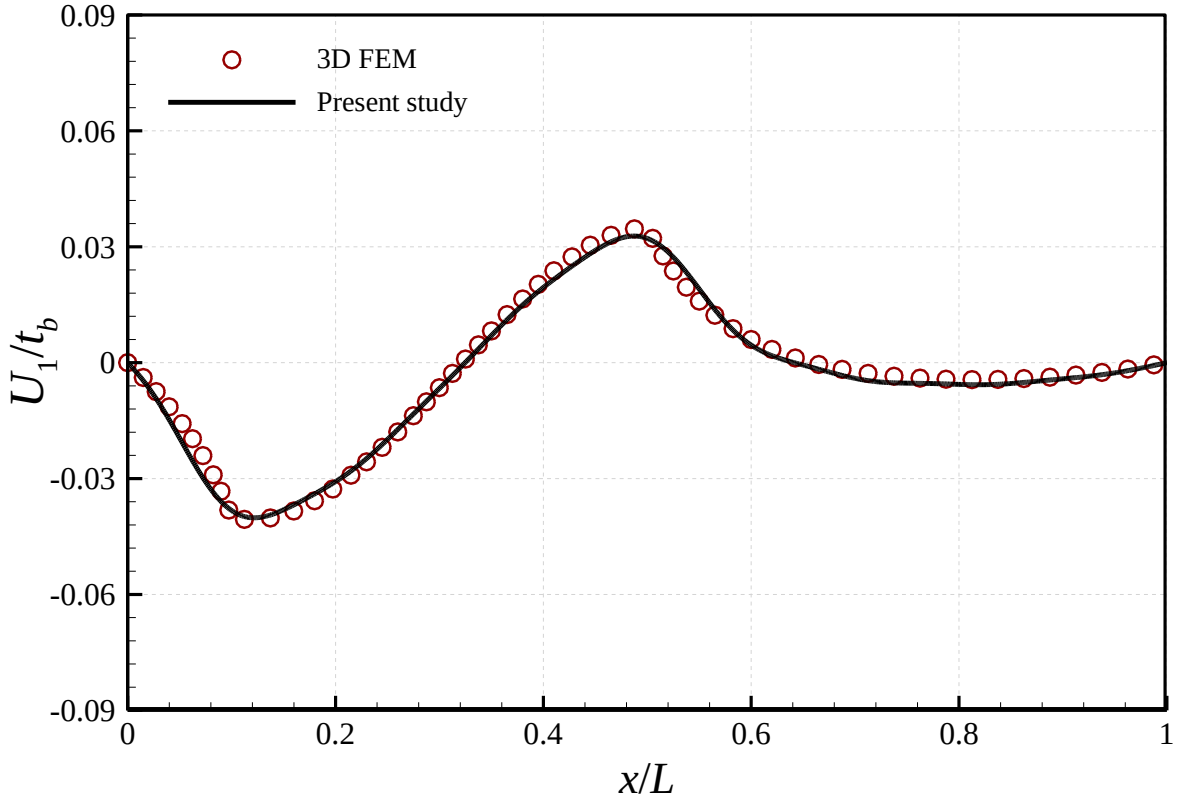

(d)

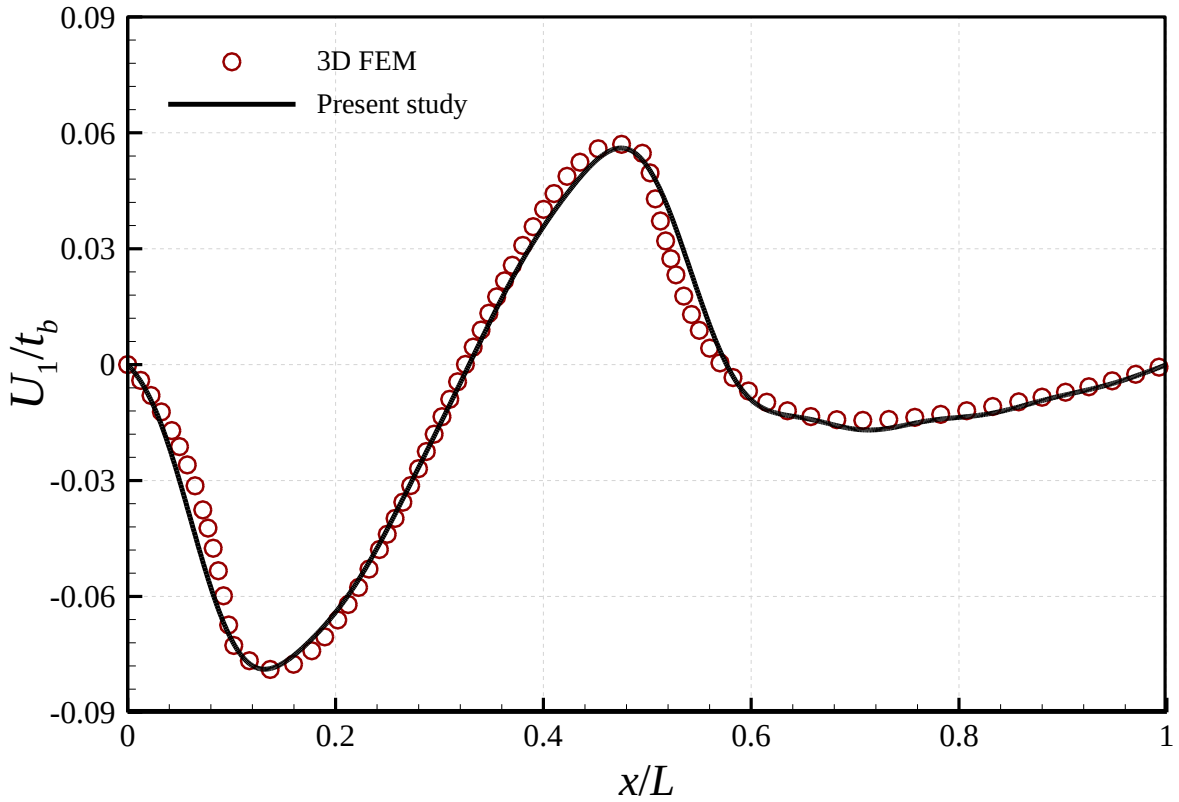

Fig.2. Nonlinear static deflection of the piezoelectrically actuated beam obtained via 3D finite element model (symbols) and the beam model developed in this study (solid line), at $z=t_b/2$: (a, b) the transverse displacement under 5 kV and 10 kV actuations, respectively; (c, d) the longitudinal displacement under 5 kV and 10 kV actuations, respectively.

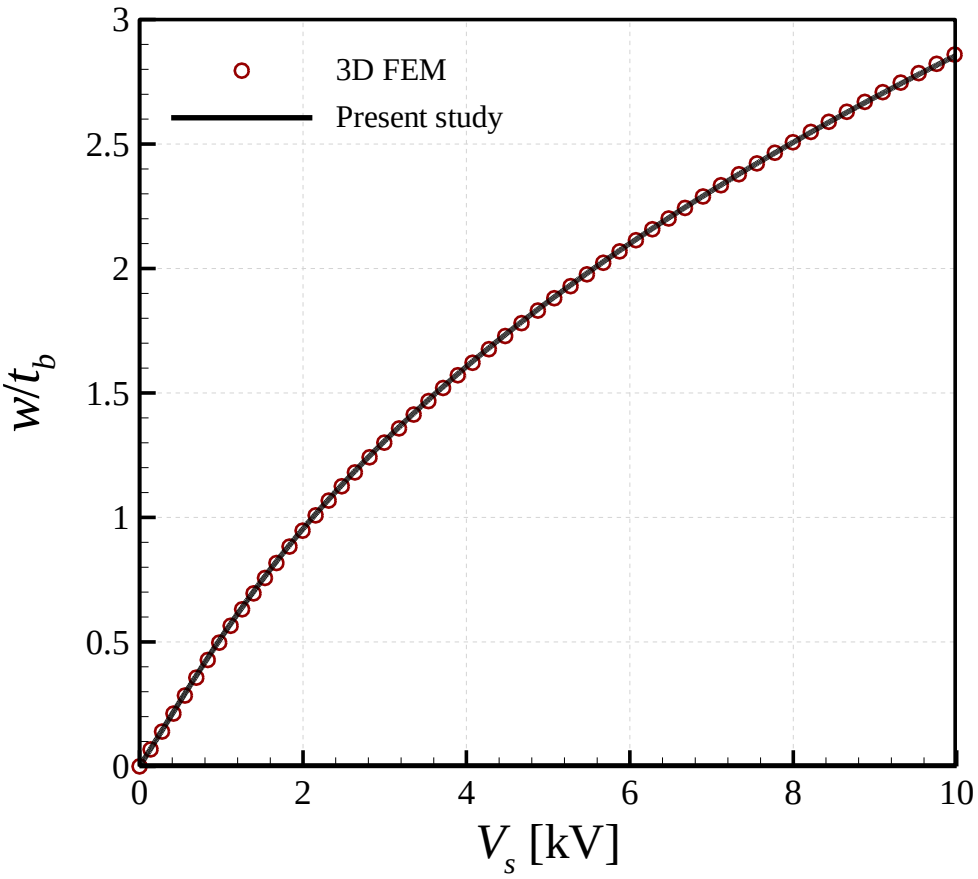

Fig.3. The nonlinear static transverse displacement at x/L=0.3 obtained via 3D finite element model (symbols) and the beam model developed in this study (solid line).

(a)

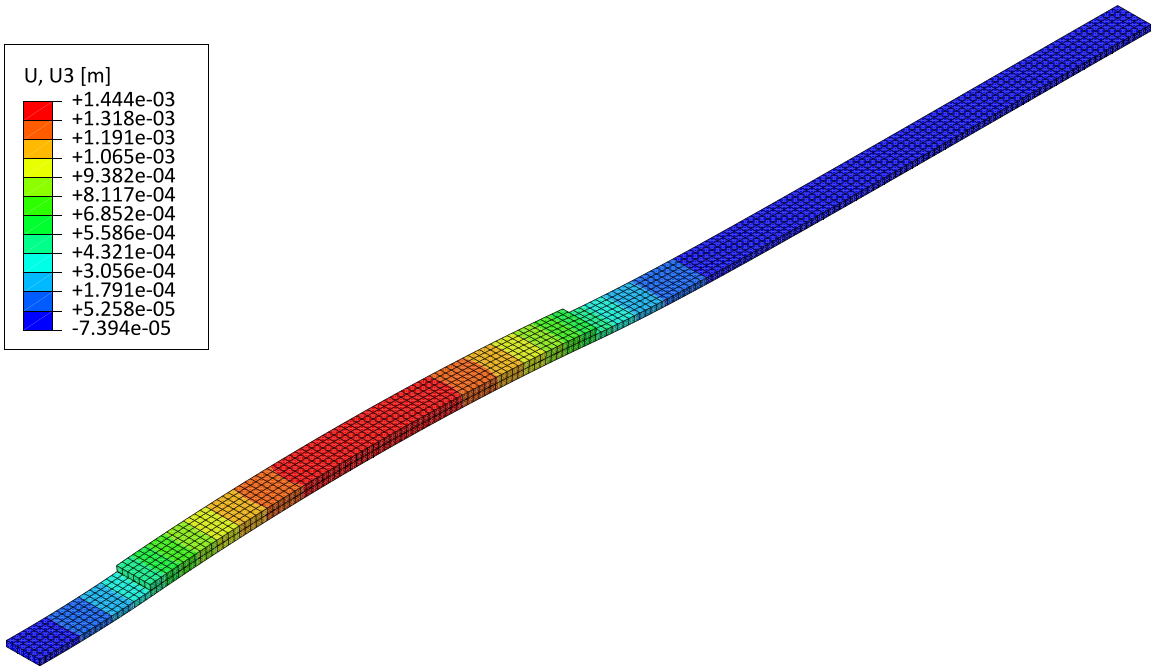

(b)

Fig.4. Finite element analysis results: (a, b) the contour plots of the transverse displacement.

(a)

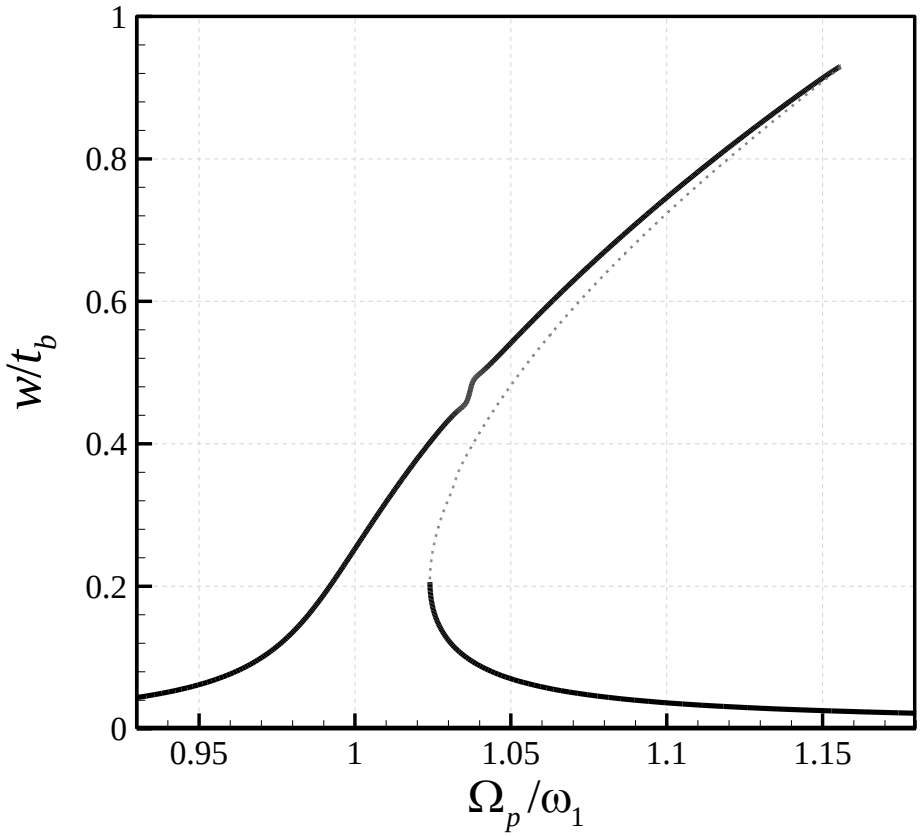

(b)

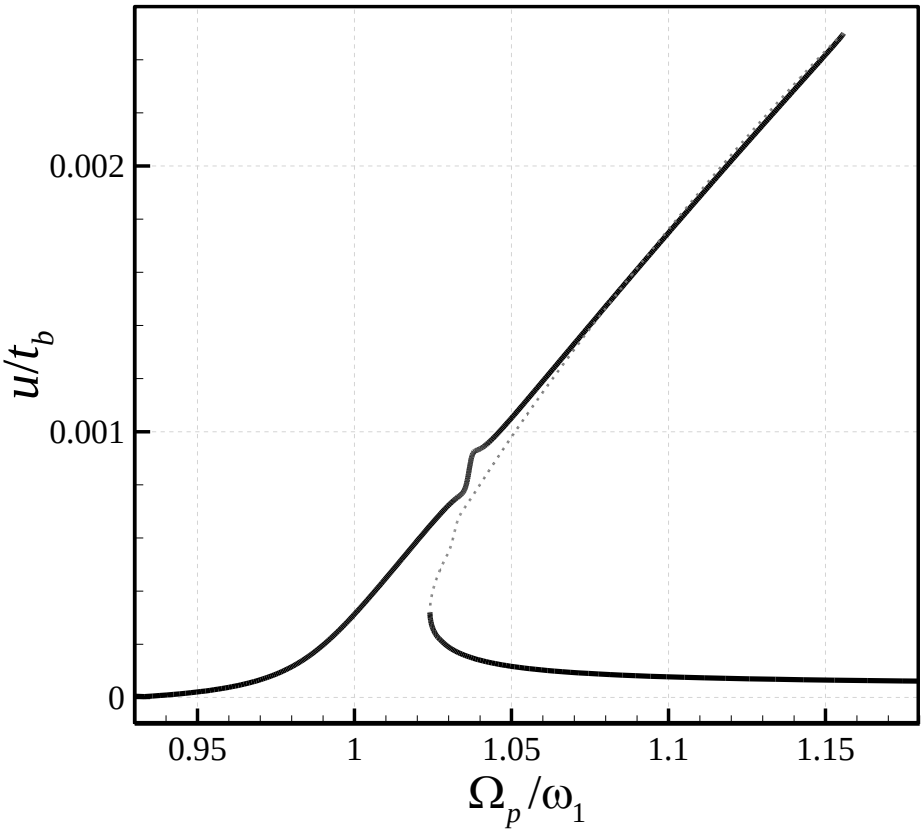

Fig.5. Primary resonance frequency-amplitude plots of the piezoelectrically actuated beam when V_d=13.0 V; (a) maximum transverse displacement at x/L=0.56; (b) maximum longitudinal displacement at x/L=0.66.

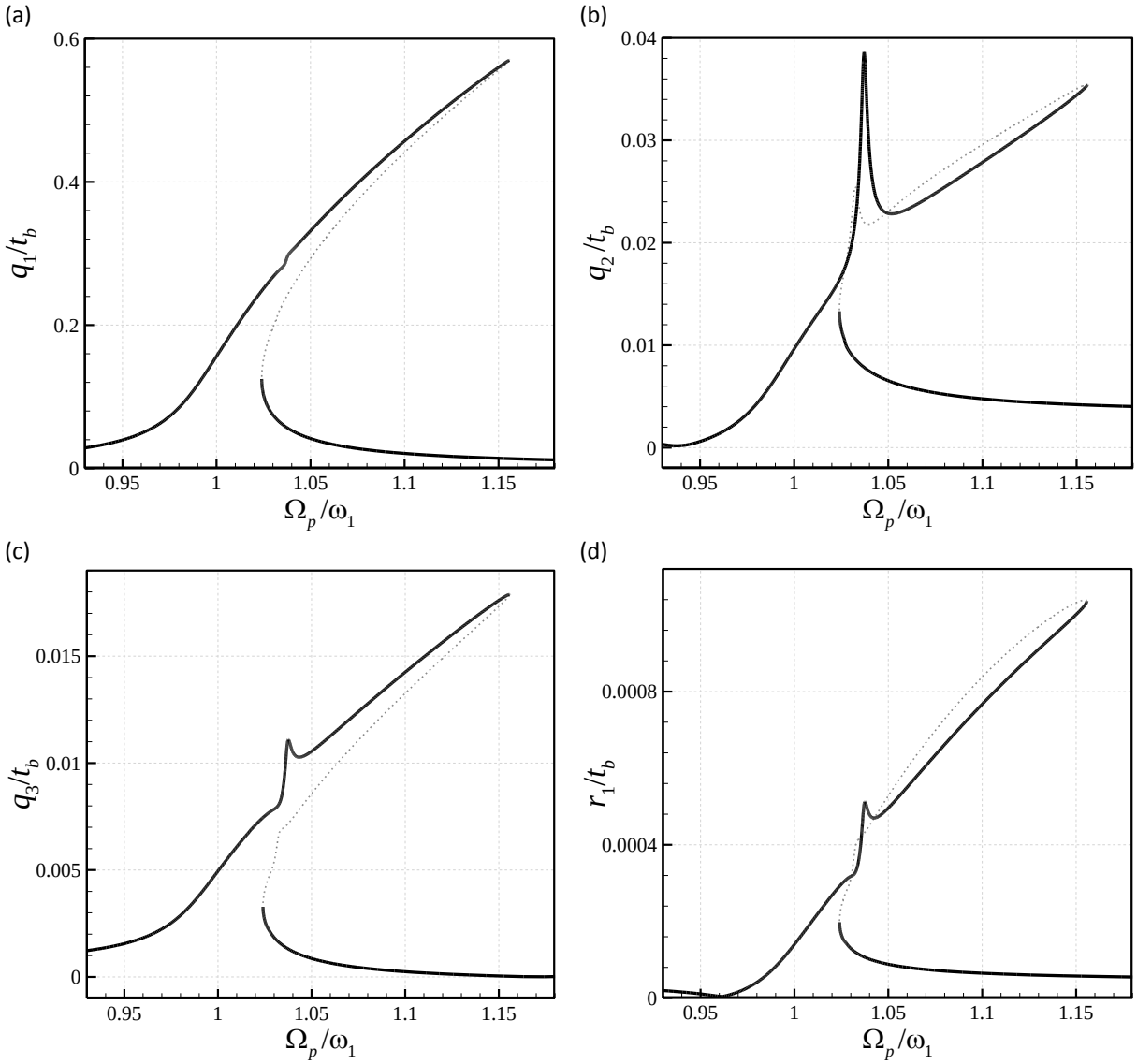

Fig.6. Frequency-amplitude plots of the system of Fig. 5, showing maximum amplitudes of the generalised coordinates q_1, q_2, q_3, and r_1.

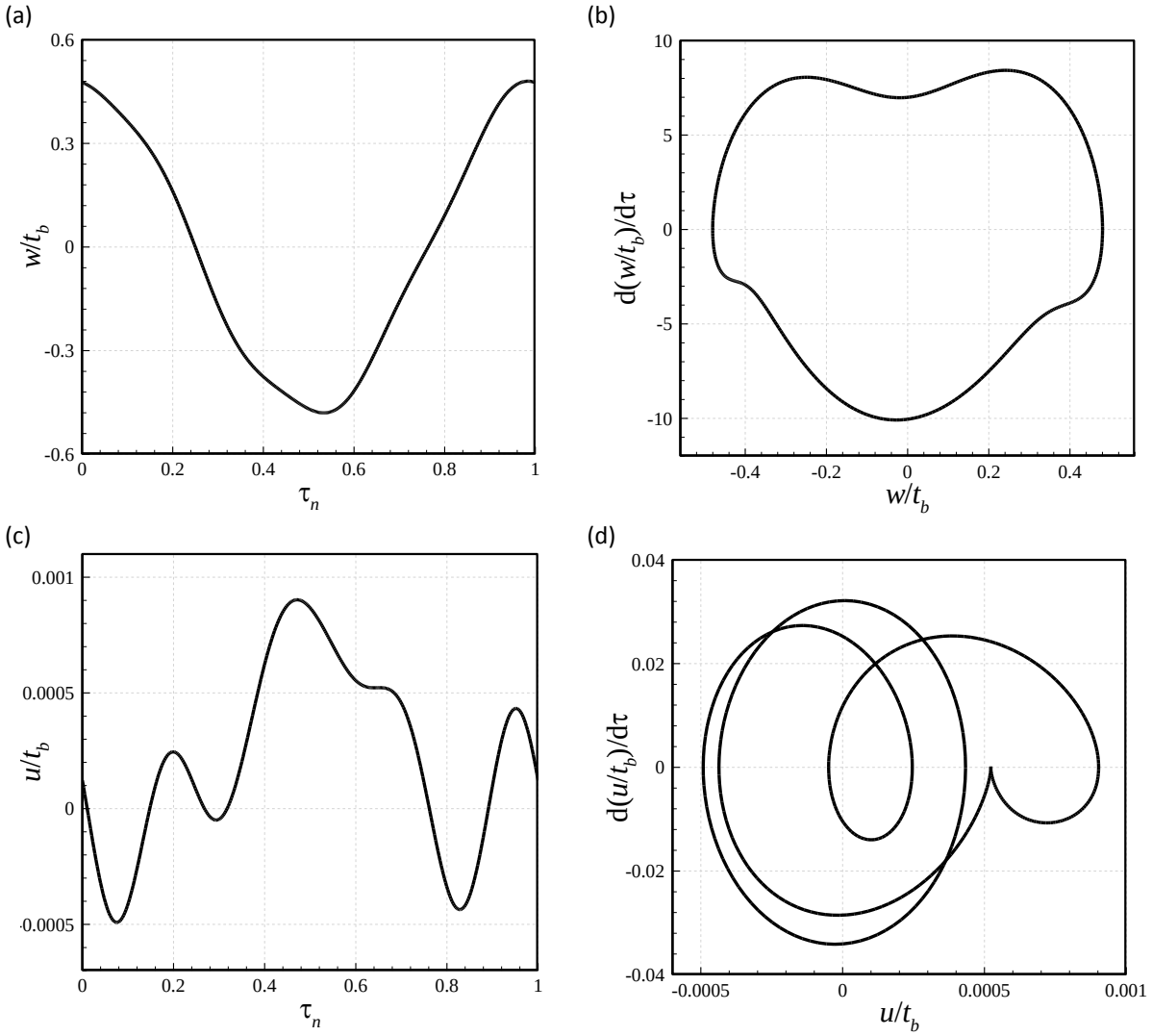

Fig.7. Motion of the system of Fig. 5 at Ω_p/ω_1=1.0373, with (a, b) showing the time trace and phase-plane portrait of the transverse displacement, and (c, d) showing those of the longitudinal displacement.

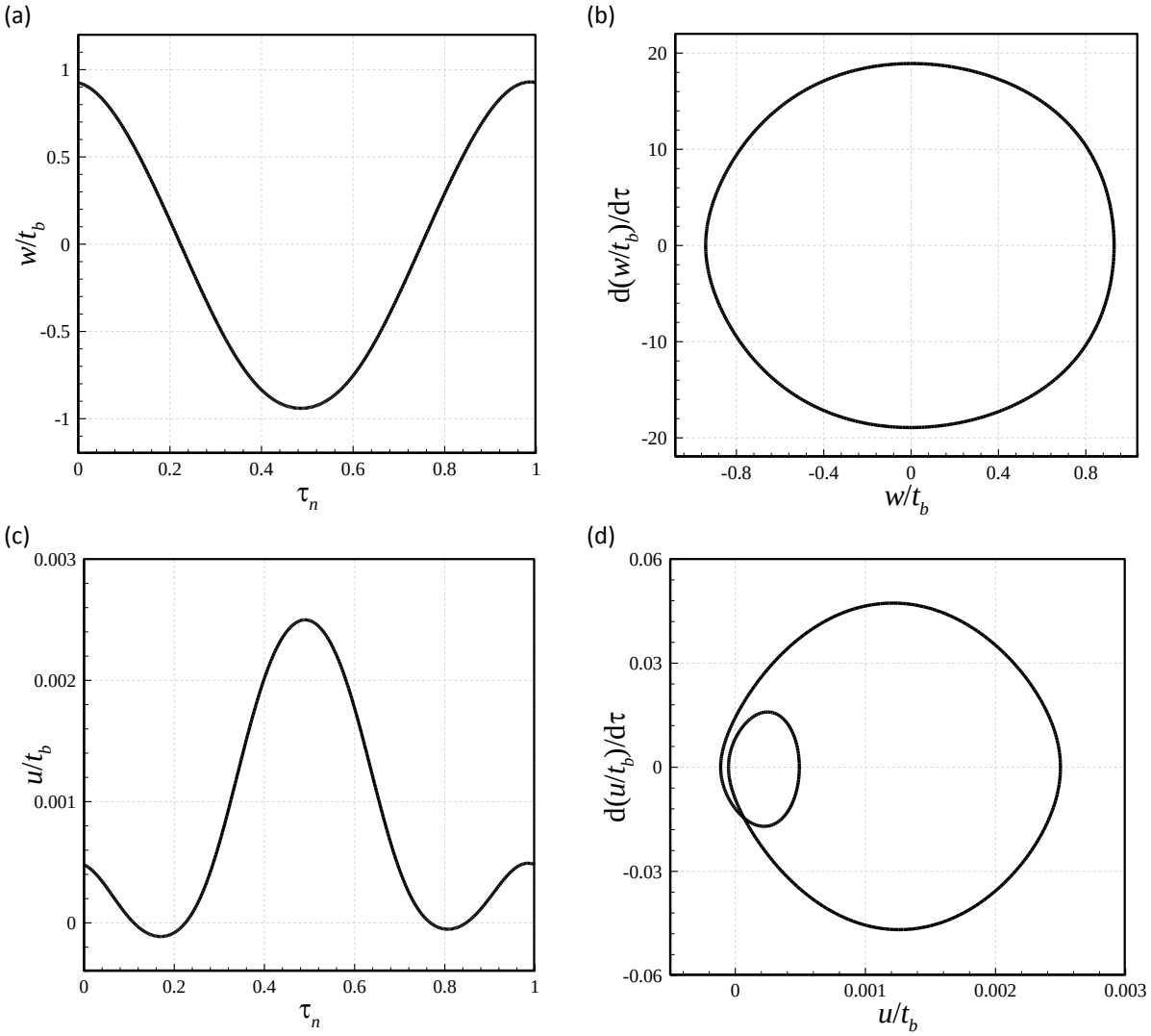

Fig.8. Motion of the system of Fig. 5 at Ω_p/ω_1=1.1558, with (a, b) showing the time trace and phase-plane portrait of the transverse displacement, and (c, d) showing those of the longitudinal displacement.

(a)

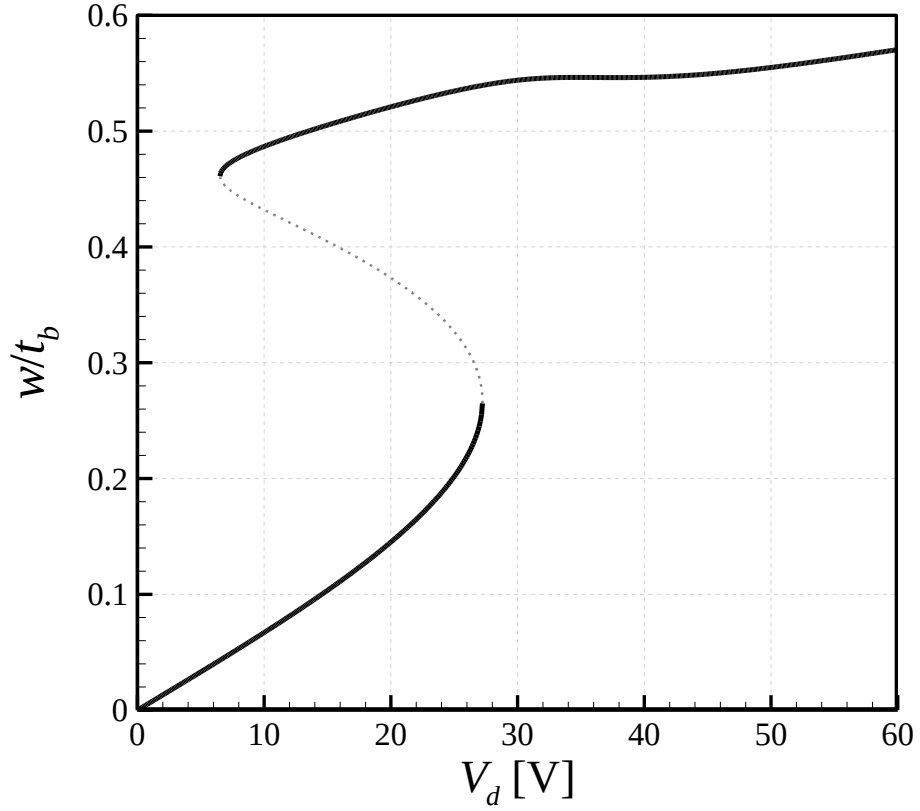

(b)

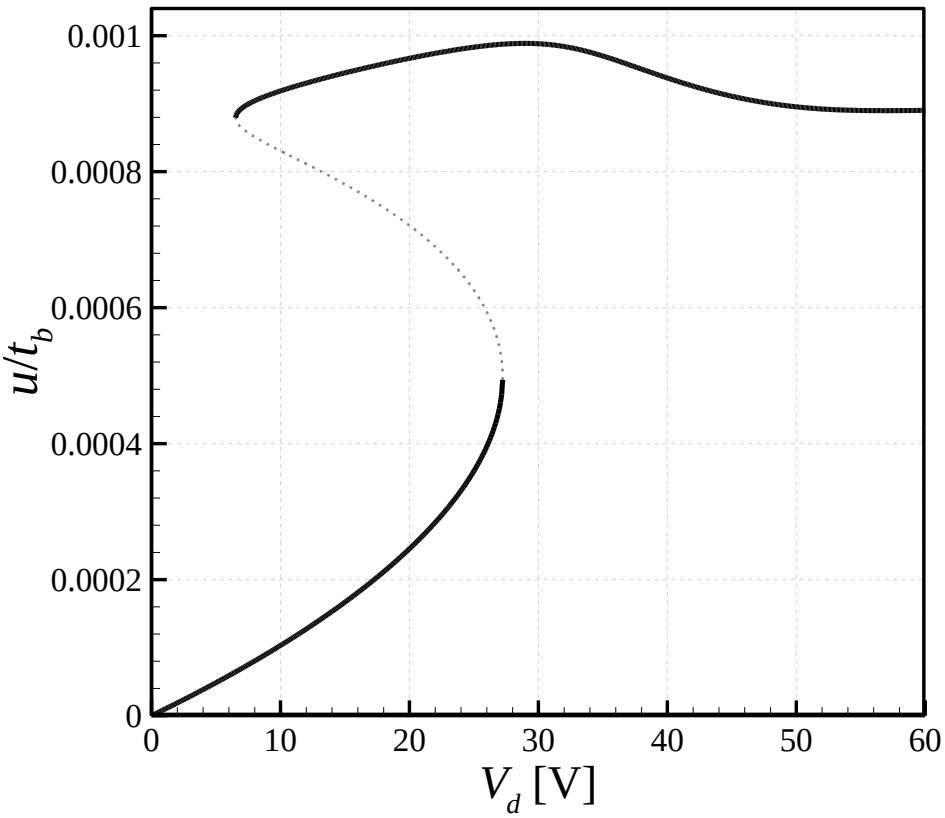

Fig.9. Force-amplitude plots of the piezoelectrically actuated beam when Ω_p/ω_1=1.04; (a) maximum transverse displacement at x/L=0.56; (b) maximum longitudinal displacement at x/L=0.66.

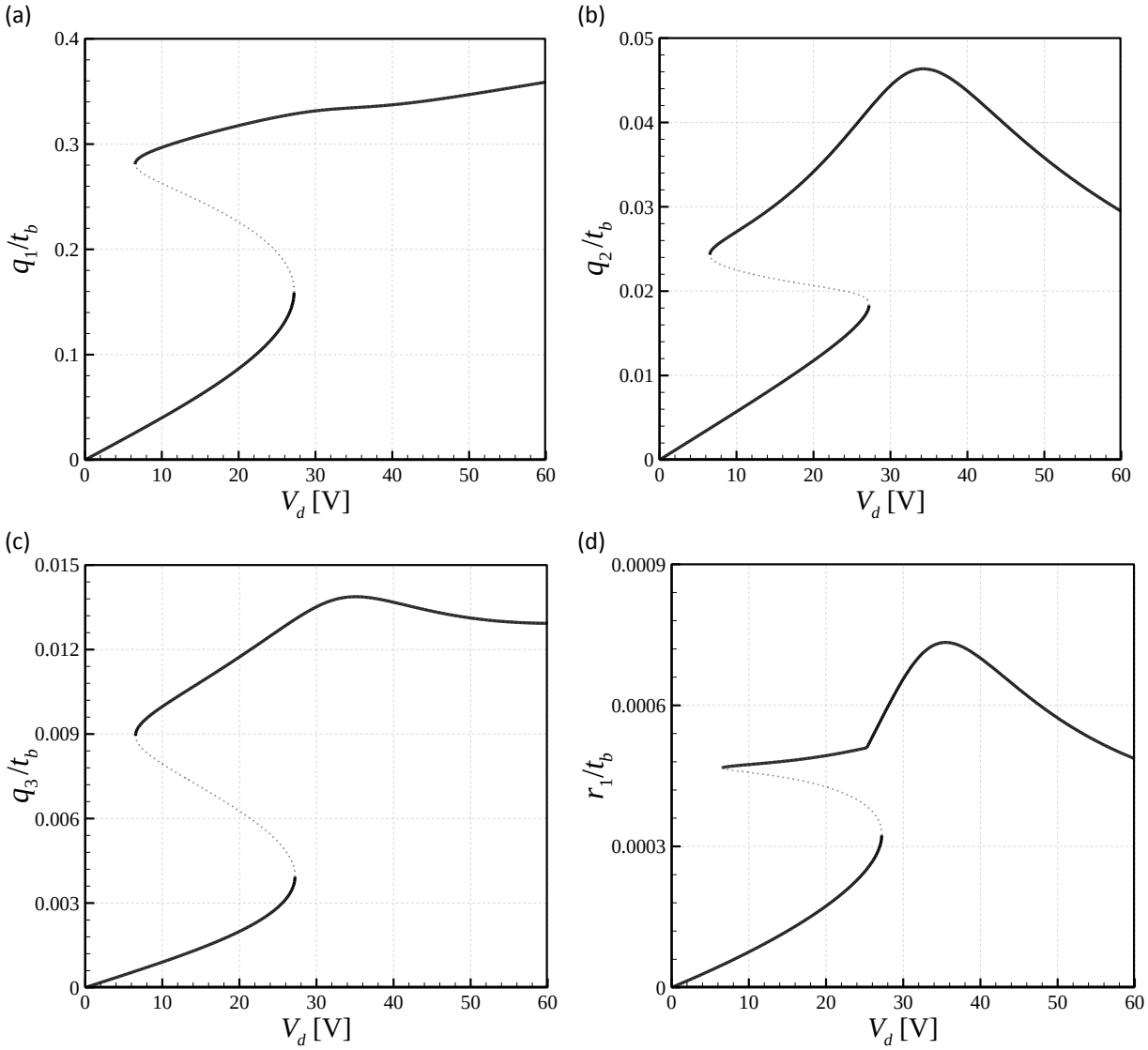

Fig.10. Force-amplitude plots of the system of Fig. 9, showing maximum amplitudes of the generalised coordinates q_1, q_2, q_3, and r_1.

(a)

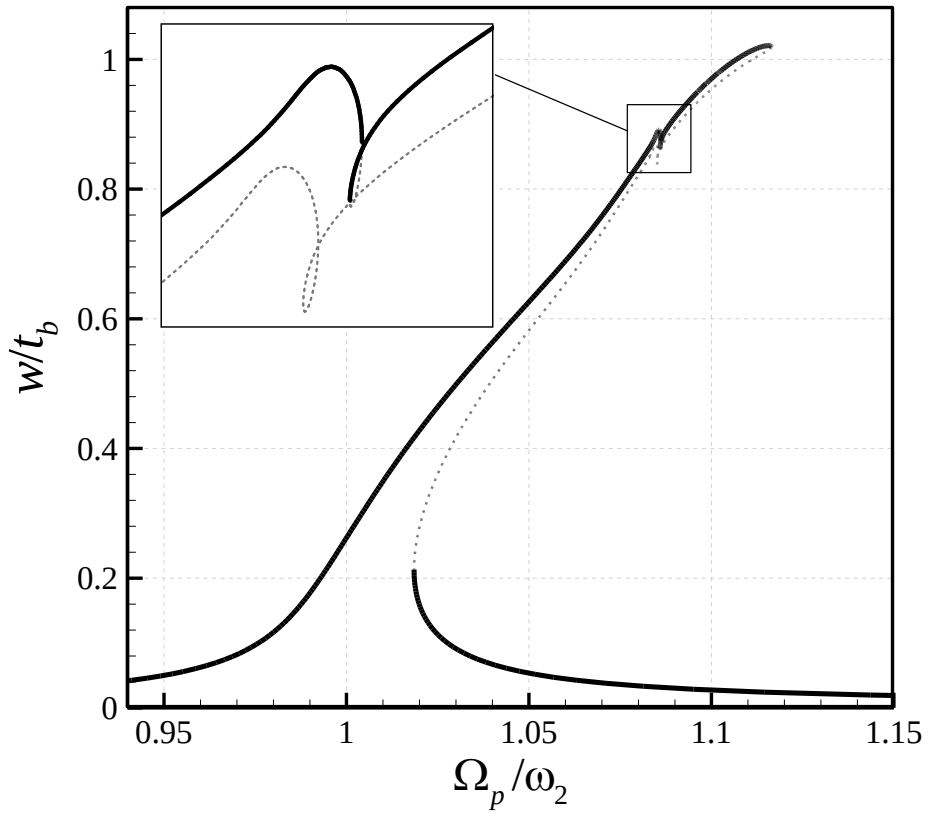

(b)

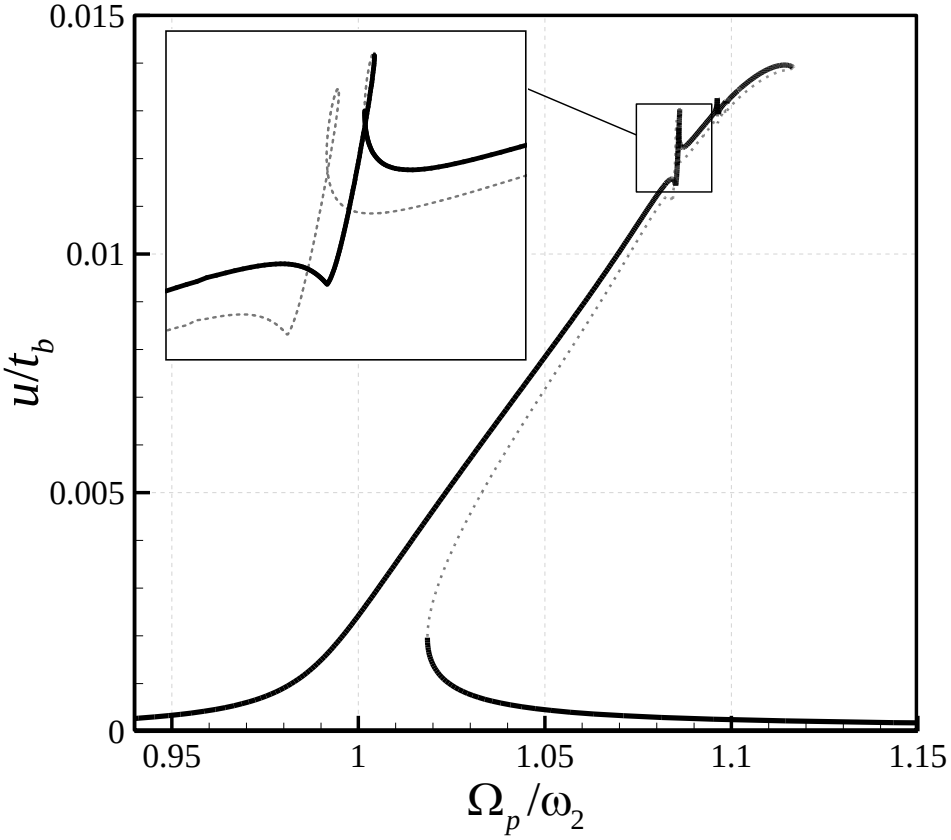

Fig.11. Secondary resonance frequency-amplitude plots of the piezoelectrically actuated beam when V_d=13.0 V; (a) maximum transverse displacement at x/L=0.81; (b) maximum longitudinal displacement at x/L=0.34.

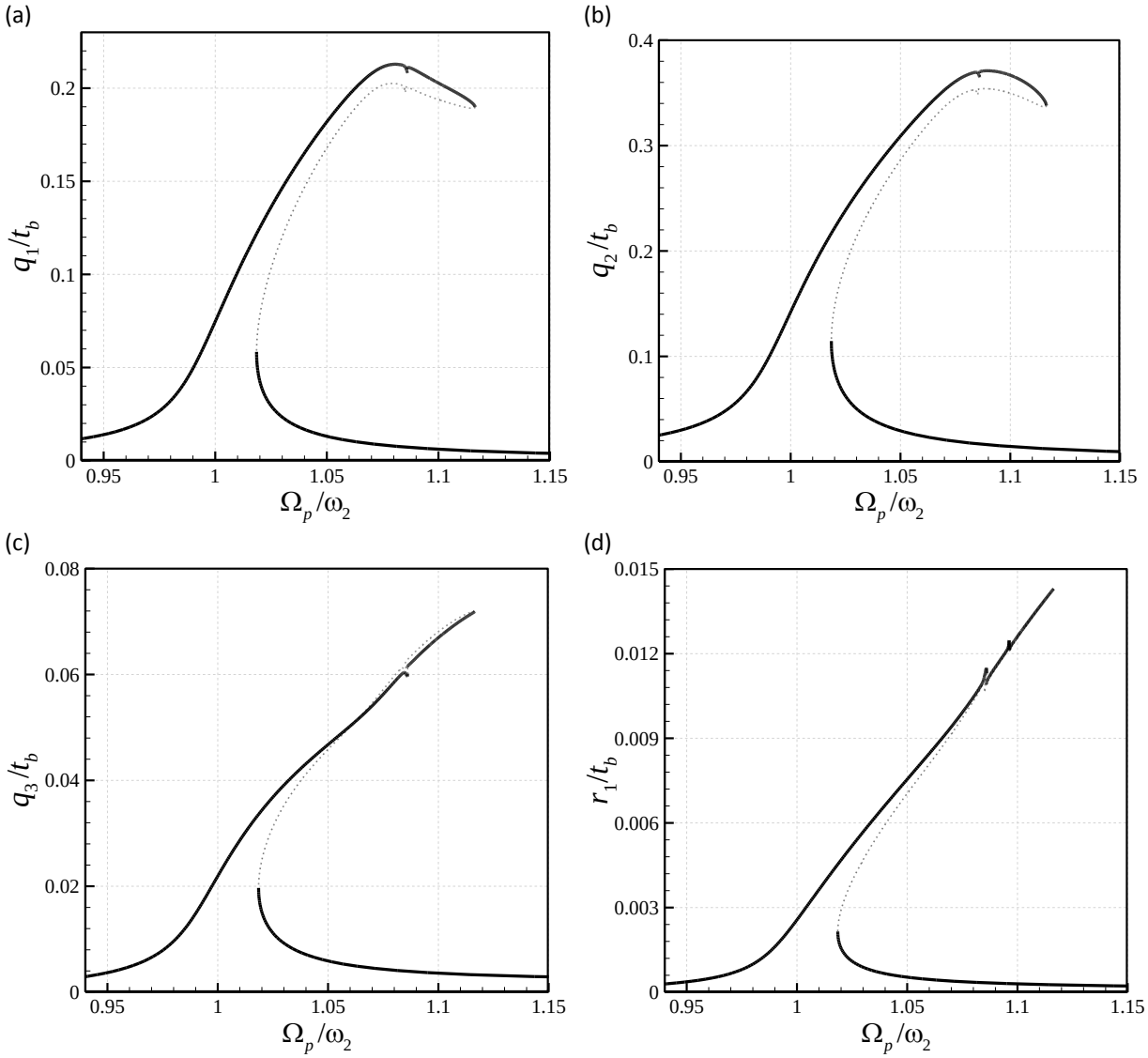

Fig.12. Frequency-amplitude plots of the system of Fig. 11, showing maximum amplitudes of the generalised coordinates q_1, q_2, q_3, and r_1.

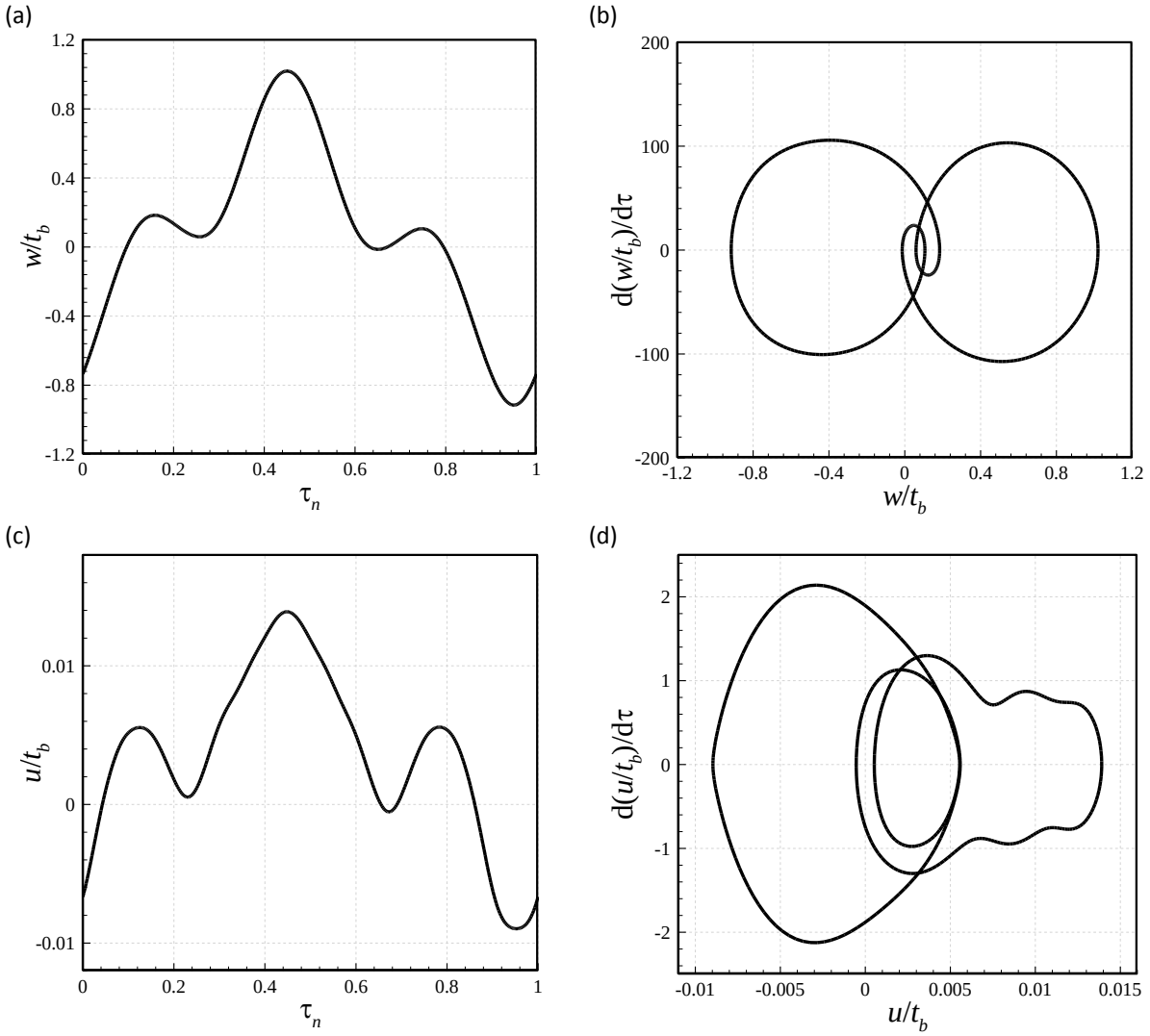

Fig.13. Motion of the system of Fig. 11 at Ω_p/ω_2=1.1164, with (a, b) showing the time trace and phase-plane portrait of the transverse displacement, and (c, d) showing those of the longitudinal displacement.

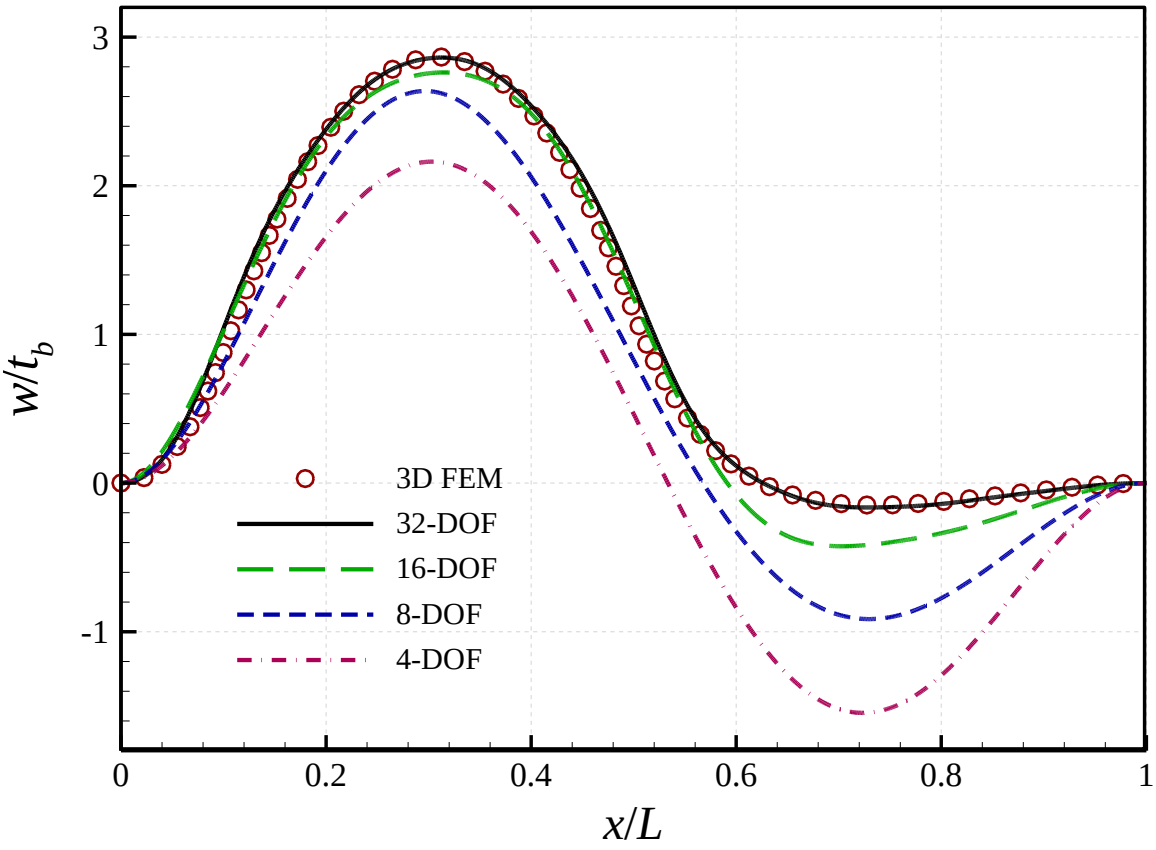

Fig.14. Nonlinear transverse deformation of the system obtained via 3D finite element model and various discretised models.